Discrete Curvature Flows for Surfaces and 3-Manifolds

Xiaotian Yin[1], Miao Jin[2], Feng Luo[3], and Xianfeng David Gu[1] ⋆

[1] Computer Science Department,
State University of New York at Stony Brook
{xyin,gu}@cs.sunysb.edu
[2] Center for Advanced Computer Studies,
University of Louisiana at Lafayette
mjin@cacs.louisiana.edu
[3] Department of Mathematics,
Rutgers University,
fluo@math.rutgers.edu

Abstract. Intrinsic curvature flows can be used to design Riemannian metrics by prescribed curvatures. This chapter presents three discrete curvature flow methods that are recently introduced into the engineering fields: the discrete Ricci flow and discrete Yamabe flow for surfaces with various topology, and the discrete curvature flow for hyperbolic 3-manifolds with boundaries. For each flow, we introduce its theories in both the smooth setting and the discrete setting, plus the numerical algorithms to compute it. We also provide a brief survey on their history and their link to some of the engineering applications in computer graphics, computer vision, medical imaging, computer aided design and others.

Key words: curvature flow, the Ricci flow, Yamabe flow, discrete, surface, 3-manifold

1 Introduction

Intrinsic curvature flows have been used in Riemannian geometry in the past 50 years with great successes. These flows deform a given Riemannian metric according to its curvature. Among the most famous ones are the *Ricci flow* and the *Yamabe flow*. Both of them can be used to design Riemannian metrics with special curvature properties.

The Ricci flow deforms the Riemannian metric according to its Ricci curvature. In particular, it can be used to find a metric with constant Ricci curvature. There is a simple physical intuition behind it. Given a compact manifold with a Riemannian metric, the metric induces the curvature function. If the metric is changed, the curvature will be changed accordingly. The metric can be deformed

⋆ This work has been supported by NSF CCF-0448399, NSF DMS-0528363, NSF DMS-0626223, NSF IIS-0713145.

in the following way: at each point, locally scale the metric, so that the scaling factor is proportional to the curvature at the point. After the deformation, the curvature will be changed. Repeating this deformation process, both the metric and the curvature will evolve like a heat diffusion. Eventually, the curvature function will become constant everywhere.

Another intrinsic curvature flow is called *Yamabe flow*. It has the same physical intuition with the Ricci flow, except for that it is driven by the scalar curvature instead of Ricci curvature. For 2-manifolds, the Yamabe flow is essentially equivalent to the Ricci flow. But for higher dimensional manifolds, Yamabe flow is much more flexible than the Ricci flow to reach constant-scalar-curvature metrics.

Due to the ability of intrinsic curvature flows on metric designs and their practical significance (see section 1.1), three special flows have been recently introduced into the engineering fields: a discrete Ricci flow on surfaces, a discrete Yamabe flow on surfaces and a discrete curvature flow on 3-manifolds. Through these work the power of curvature flows has been extended from the pure theoretical study to solving practical problems.

1.1 Motivations

Curvature flows have played critical roles in the study of differential geometry for a long time. One of the most recent examples appears in the proof of the Poincaré conjecture on 3-manifolds [Per02,Per03b,Per03a], where the Ricci flow is employed as a fundamental tool.

Besides that, intrinsic curvature flows also turn out to be able to help solve many practical problems in engineering fields, especially those that can be formulated as finding certain metrics with desired properties.

In graphics, a surface parametrization is commonly used, which refers to the process of mapping a given surface to a canonical domain. If the domain is planar, then it is equivalent to finding a Riemannian metric that induces zero Gaussian curvature everywhere. Such a metric is called a flat metric.

In digital geometry processing, if such a parameterization is known, any signal (e.g. texture) on the surface can be defined on the parametric domain. Complicated processing tasks on surfaces can be simplified to easier ones on the parametric domains, such as texturing [LPRM02] and re-meshing [AMD02].

In computer-aided geometric modeling, a flat metric is helpful for constructing manifold splines, whose parametric domains are manifolds with arbitrary topologies instead of planar domains. In order to build a manifold spline, a special atlas of the domain manifold is required, such that all local coordinate transition maps are affine. One way to construct such an atlas is to find a flat metric. Details of the manifold theory and the construction of an affine atlas can be found in [GHQ06].

In the medical imaging field, conformal brain mapping has been widely used, which maps the human brain cortical surfaces to the unit sphere to facilitate registration, fusion, and comparison. This is equivalent to finding a Riemannian metric on the brain cortical surface, such that the induced Gaussian curvature is a constant $+1$ everywhere.

For 3-manifolds, discrete curvature flow is also valuable, not only for the theoretical investigation of their topological structures and geometric properties, but also for many engineering applications over them, such as volumetric parameterization, registration, shape analysis and so on.

One should note that, in engineering fields manifolds are usually approximated using discrete constructions, such as piece-wise linear meshes; in order to employ curvature flow to solve practical problems, we need to extend the theories of curvature flows from the smooth setting to the corresponding discrete setting, and need to pay attention to the convergence of the later to the former. Based on the discrete theories and formula, one is allowed to design computer algorithms which can simulate and compute the flow.

1.2 A Brief History

The theory of intrinsic curvature flows originated from differential geometry, and were later introduced into the engineering fields. In this section, we give a brief overview of the literature that are directly related to the three flows mentioned above. For each flow, we would introduce some representative work on three aspects: theories in the smooth setting, theories in the discrete setting and computer algorithms to compute the flow.

The Ricci flow on surfaces The Ricci flow was introduced by R. Hamilton in a seminal paper [Ham82] for Riemannian manifolds of any dimension. The Ricci flow has revolutionized the study of geometry of surfaces and 3-manifolds and has inspired huge research activities in geometry. In particular, it leads to a proof of the 3-dimensional Poincaré conjecture. In the paper [Ham88], Hamilton used the 2-dimensional Ricci flow to give a proof of the uniformization theorem for surfaces of positive genus. This leads a way for potential applications to computer graphics.

There are many ways to discretize smooth surfaces. The one which is particularly related to a discretization of conformality is the circle packing metric introduced by Thurston [Thu80]. The notion of circle packing has appeared in the work of Koebe [Koe36]. Thurston conjectured in [Thu85] that for a discretization of the Jordan domain in the plane, the sequence of circle packings converge to the Riemann mapping. This was proved by Rodin and Sullivan [RS87].

Colin de Verdiere [dVY91] established the first variational principle for circle packing and proved Thurston's existence of circle packing metrics. This paved a way for a fast algorithmic implementation of finding the circle packing metrics, such as the one by Collins and Stephenson [CS03]. In [CL03], Chow and Luo generalized Colin de Verdiere's work and introduced the discrete Ricci flow and discrete Ricci energy on surfaces. They proved a general existence and convergence theorem for the discrete Ricci flow and proved that the Ricci energy is convex. The algorithmic implementation of the discrete Ricci flow was carried out by Jin et al [JKLG08].

Another related discretization method is called circle pattern; it considers both the combinatorics and the geometry of the original mesh, and can be looked as a variant to circle packings. Circle pattern was proposed by Bowers and Hurdal [BH03], and has been proven to be a minimizer of a convex energy by Bobenko and Springborn [BS04]. An efficient circle pattern algorithm was developed by Kharevych et al [KSS06].

The Yamabe flow on surfaces The Yamabe problem aims at finding a conformal metric with constant scalar curvature for compact Riemannian manifolds. The first proof (with flaws) was given by Yamabe [Yam60], which was corrected and extended to a complete proof by several researchers including Trudinger [Tru68], Aubin [Aub76] and Schoen [Sch84]. A comprehensive survey on this topic was given by Lee and Parker in [LP87].

In [Luo04] Luo studied the discrete Yamabe flow on surfaces. He introduced a notion of discrete conformal change of polyhedral metric, which plays a key role in developing the discrete Yamabe flow and the associated variational principle in the field. Based on the discrete conformal class and geometric consideration, Luo gave the discrete Yamabe energy as an integration of a differential 1-form and proved that this energy is a locally convex function. He also deduced from it that the curvature evolution of the Yamabe flow is a heat equation.

In a very nice recent work of Springborn et al [SSP08] they were able to identify the Yamabe energy introduced by Luo with the Milnor-Lobachevsky function and the heat equation for the curvature evolution with the cotangent Laplace equation. They constructed an algorithm based on their explicit formula. Another recent work by Gu et al [CCG], which used the original discrete Yamabe energy from [Luo04], has produced an equally efficient algorithm in finding the discrete conformal metrics.

A curvature flow on 3-manifolds Due to the drastic difference between the geometry of 3-manifolds and that of 2-manifolds, it turns out that the study of curvature flows is much more complicated on the former than on the later. This is also reflected by the fact that it is harder and slower for the discrete curvature flow on 3-manifolds to be introduced into the engineering fields than that on 2-manifolds.

The very first work of the Ricci flow on 3-manifolds was given by Hamilton in his seminal paper [Ham82]. Following this line Perelman was able to apply the Ricci flow to prove the Poincaré conjecture and Thurston's geometrization conjecture in [Per02,Per03b,Per03a]. Inspired by the ideas from [Ham82], Luo introduced the discrete curvature flow on a special class of compact 3-manifolds whose boundary is consisting of surfaces of negative Euler characteristic. In a very recent work by Yin et al [YJLG08], they developed an algorithm to compute the discrete curvature flow and visualize the constant-curvature metrics on such 3-manifolds.

The rest of the chapter is organized as follows. We first introduce some basic concepts and theories of the surface Ricci flow in both the smooth setting (section 2) and the discrete setting (section 3), which is followed by the numerical algorithms to compute the flow (section 4). In section 5 we present the discrete algorithm of surface Yamabe flow. The discrete curvature flow on 3-manifolds with boundaries are introduced in section 6 and the numerical algorithm is presented in 7. Further details on discrete curvature flows and their variational principles can be found in [LGD07]. The details and source codes of the algorithms presented here can be found in [GY08] and [CCG].

2 Theories on The Smooth Surface Ricci Flow

In this section, we introduce the theory of the Ricci flow in the continuous setting, which will be extended to the discrete setting in 3.

2.1 Fundamental Group and Universal Covering Space

The closed loops on the surface can be classified by homotopy equivalence. If two closed curves on a surface M can deform to each other without leaving the surface, then they are *homotopic* to each other. Two closed curves sharing common points can be concatenated to form another loop. This operation defines the multiplication of homotopic classes. All the homotopy classes form the so called *first fundamental group* of M. A collection of curves on the surface is a *cut graph*, if their complement is a topological disk, which is called the *fundamental domain* of the surface.

For a genus g closed surface, the fundamental group has $2g$ generators. A set of fundamental group basis $\{a_1, b_1, a_2, b_2, \cdots, a_g, b_g\}$ is *canonical*, if a_i, b_i have only one geometric intersection, but neither a_i, a_j nor a_i, b_j have geometric intersections, where $i \neq j$. Figs. 8(a) and 6(a) show the sets of canonical fundamental group generators for the kitten model with zero Euler number and the amphora model with negative Euler number. If we slice M along the curves, we can get a disk-like domain with boundary $\{a_1 b_1 a_1^{-1} b_1^{-1} a_2 b_2 a_2^{-1} b_2^{-1} \cdots a_g b_g a_g^{-1} b_g^{-1}\}$, which is called the *canonical fundamental domain* of the surface M.

A covering space of M is a surface $\bar{M}$ together with a continuous surjective map $p : \bar{M} \to M$, such that for every $q \in M$ there exists an open neighborhood U of q such that $p^{-1}(U)$ (the inverse image of U under p) is a disjoint union of open sets in $\bar{M}$, each of which is mapped homeomorphically onto U by p. If $\bar{M}$ is simply connected, then $\bar{M}$ is called the *universal covering space* of M. Suppose $\phi : \bar{M} \to \bar{M}$, $p = \phi \circ p$, then ϕ is called a *deck transformation.* A deck transformation maps one fundamental domain to another fundamental domain. All the deck transformations form the so-called *deck transformation group*, which is isomorphic to the fundamental group. We use the algorithms in [CJGQ05] to compute the canonical fundamental group generators.

2.2 Riemannian Metric and Gaussian Curvature

All the differential geometric concepts and the detailed explanations can be found in [Gug77]. Suppose S is a C^2 smooth surface embedded in $\mathbb{R}^3$ with local parameter (u_1, u_2). Let $\mathbf{r}(u_1, u_2)$ be a point on S and $d\mathbf{r} = \mathbf{r}_1 du_1 + \mathbf{r}_2 du_2$ be the tangent vector defined at that point, where $\mathbf{r}_1, \mathbf{r}_2$ are the partial derivatives of $\mathbf{r}$ with respect to u_1 and u_2, respectively. The *Riemannian metric* or the *first fundamental form* is:

$$< d\mathbf{r}, d\mathbf{r} >= \sum < \mathbf{r}_i, \mathbf{r}_j > du_i du_j, \quad i, j = 1, 2. \tag{1}$$

The Gauss map $G : S \to \mathbb{S}^2$ from the surface S to the unit sphere $\mathbb{S}^2$ maps each point p on the surface to its normal $\mathbf{n}(p)$ on the sphere. The *Gaussian curvature $K(p)$ is defined as the Jacobian of the Gauss map.* Intuitively, it is the ratio between the infinitesimal area of the Gauss image on the Gaussian sphere and the infinitesimal area on the surface.

Let ∂S be the boundary of the surface S, k_g the geodesic curvature, dA the area element, ds the line element, and $\chi(S)$ the Euler characteristic number of S. The total curvature is determined by the topology:

$$\int_S K dA + \int_{\partial S} k_g ds = 2\pi\chi(S). \tag{2}$$

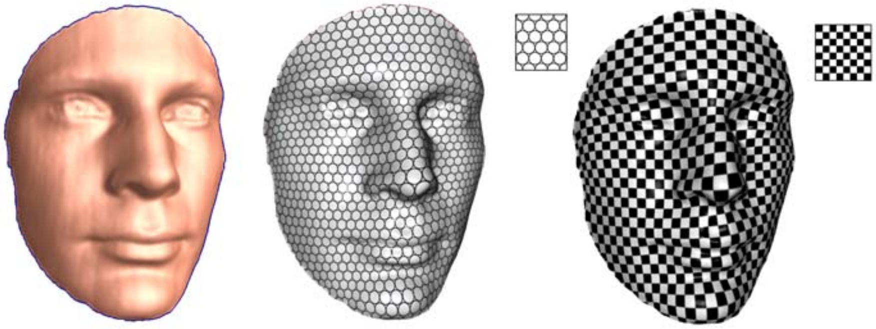

Fig. 1. Properties of Conformal Mapping: Conformal mappings transform infinitesimal circles to infinitesimal circles and preserve the intersection angles among the circles. Here, infinitesimal circles are approximated by finite ones. Notice that a circle in the texture appears in a scaled one in the texture mapping result. Also, the angles in the checkerboard pattern preserved in the texture mapping result.

2.3 Conformal Deformation

Let S be a surface embedded in $\mathbb{R}^3$. S has a Riemannian metric induced from the Euclidean metric of $\mathbb{R}^3$, denoted by $\mathbf{g}$. Suppose $u : S \to \mathbb{R}$ is a scalar function defined on S. It can be verified that $\bar{\mathbf{g}} = e^{2u}\mathbf{g}$ is also a Riemannian metric on S. Furthermore, angles measured by $\mathbf{g}$ are equal to those measured by $\bar{\mathbf{g}}$. Therefore, we say $\bar{\mathbf{g}}$ is a *conformal deformation* from $\mathbf{g}$.

A conformal deformation maps infinitesimal circles to infinitesimal circles and preserves the intersection angles among the infinitesimal circles. In Fig. 1, we illustrate this property by approximating infinitesimal circles by finite circles. We put a regular circle packing pattern on the texture and map the texture to the surface using a conformal parameterization, where all the circles on the texture still look like circles on the surface, and all the tangency relations among the circles are preserved.

When the Riemannian metric is conformally deformed, curvatures will also be changed accordingly. Suppose $\mathbf{g}$ is changed to $\bar{\mathbf{g}} = e^{2u}\mathbf{g}$. Then, the Gaussian curvature will become

$$\bar{K} = e^{-2u}(-\Delta_{\mathbf{g}} u + K), \tag{3}$$

where $\Delta_{\mathbf{g}}$ is the Laplacian-Beltrami operator under the original metric $\mathbf{g}$. The geodesic curvature will become

$$\bar{k} = e^{-u}(\partial_{\mathbf{r}} u + k), \tag{4}$$

where $\mathbf{r}$ is the tangent vector orthogonal to the boundary. According to the Gauss-Bonnet theorem, the total curvature is still $2\pi\chi(S)$, where $\chi(S)$ is the Euler characteristic number of S.

2.4 Uniformization Theorem

Given a surface S with a Riemannian metric $\mathbf{g}$, there exists infinitely many metrics conformal to $\mathbf{g}$. The following uniformization theorem states that, among all of the conformal metrics, there exists a representative, which induces constant curvature. Moreover, the constant will be one of $\{+1, 0, -1\}$.

Theorem 1 (Uniformization Theorem). *Let* $(S, \mathbf{g})$ *be a compact 2-dimensional surface with a Riemannian metric* $\mathbf{g}$*, then there is a metric* $\bar{\mathbf{g}}$ *conformal to* $\mathbf{g}$ *with constant Gaussian curvature everywhere; the constant is one of* $\{+1, 0, -1\}$*. Furthermore, the constant* -1 *curvature metric is unique.*

We call such a metric the *uniformization metric* of S. According to the Gauss-Bonnet theorem (Eq. 2), the sign of the constant Gaussian curvature must match the sign of the Euler number of the surface: $+1$ for $\chi(S) > 0$, 0 for $\chi(S) = 0$, and -1 for $\chi(S) < 0$.

Therefore, we can embed the universal covering space of any closed surface using its uniformization metric onto one of the three canonical surfaces: the *sphere* $\mathbb{S}^2$ for genus zero surfaces with positive Euler numbers, the *plane* $\mathbb{E}^2$ for genus one surfaces with zero Euler number, and the *hyperbolic space* $\mathbb{H}^2$ for high genus surfaces with negative Euler numbers (see Fig. 2). Accordingly, we can say that surfaces with positive Euler number admit spherical geometry; surfaces with zero Euler number admit Euclidean geometry; and surfaces with negative Euler number admit hyperbolic geometry.

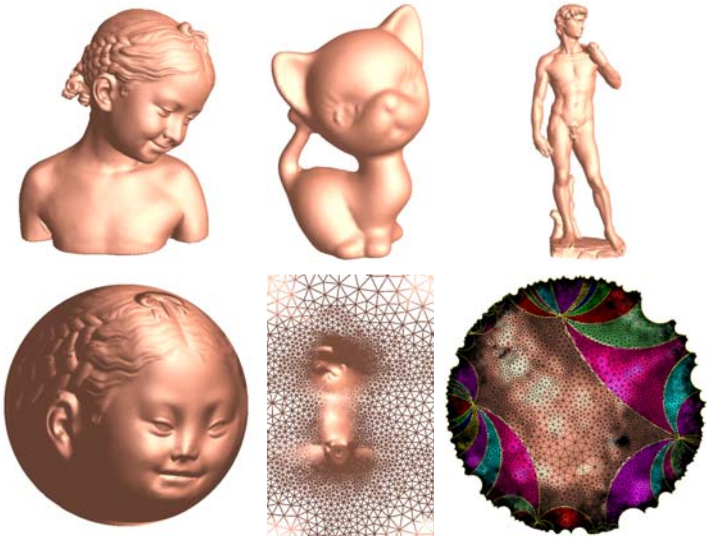

(a) $\chi > 0,\ \mathbb{S}^2$ (b) $\chi = 0,\ \mathbb{E}^2$ (c) $\chi < 0,\ \mathbb{H}^2$

Fig. 2. Uniformization Theorem: Each surface in $\mathbb{R}^3$ admits a uniformization metric, which is conformal to the original metric and induces constant Gaussian curvature; the constant is one of $\{+1, 0, -1\}$ depending on the Euler characteristic number χ of the surface. Its universal covering space with the uniformization metric can be isometrically embedded onto one of three canonical spaces: sphere, plane, or hyperbolic space. Here, we shows the parameterizations computed by using discrete spherical, Euclidean, and hyperbolic Ricci flows, respectively.

2.5 Spherical, Euclidean and Hyperbolic Geometry

The unit sphere is with Gaussian curvature +1 and admits the spherical geometry. The rigid motions in spherical geometry are rotations. The geodesics are great arcs. The Euclidean plane is with 0 curvature and admits the Euclidean geometry. Planar translations and rotations form the rigid motion group.

The hyperbolic space model we used in this paper is the Poincaré disk, which is a unit disk on the complex plane, with Riemannian metric

$$ds^2 = \frac{4dwd\bar{w}}{(1-\bar{w}w)^2}, w \in \mathbb{C}.$$

In the Poincaré disk, rigid motion is a Möbius transformation,

$$z \to e^{i\theta}\frac{z - z_0}{1 - \bar{z}_0 z}, z_0 \in \mathbb{C}, \theta \in [0, 2\pi);$$

the geodesics are circular arcs which are orthogonal to the unit circle; the hyperbolic circle $(\mathbf{c}, r)$ ($\mathbf{c}$ represents the center, r the radius) coincides with an Euclidean circle $(\mathbf{C}, R)$ with

$$\mathbf{C} = \frac{2 - 2\mu^2}{1 - \mu^2|\mathbf{c}|^2}\mathbf{c}, \quad R^2 = |\mathbf{C}|^2 - \frac{|\mathbf{c}|^2 - \mu^2}{1 - \mu^2|\mathbf{c}|^2},$$

where $\mu = \frac{e^r - 1}{e^r + 1}$.

We also use the upper half plane model for hyperbolic space $\mathbb{H}^2$. $\mathbb{H}^2 = \{(x, y) \in \mathbb{R}^2 | y > 0\}$, with the Riemannian metric $ds^2 = \frac{dx^2 + dy^2}{y^2}$. In $\mathbb{H}^2$, hyperbolic lines are circular arcs and half lines orthogonal to the x-axis. The rigid motion is given by the so-called *Möbius transformation*

$$\frac{az + b}{cz + d}, ac - bd = 1, a, b, c, d \in \mathbb{R},$$

where $z = x + iy$ is the complex coordinates.

Similarly, the three dimensional hyperbolic space $\mathbb{H}^3$ can be represented using upper half space model,$\mathbb{H}^3 = \{(x, y, z) \in \mathbb{R}^3 | z > 0\}$, with Riemannian metric

$$ds^2 = \frac{dx^2 + dy^2 + dz^2}{z^2}.$$

In $\mathbb{H}^3$, the hyperbolic planes are hemispheres or vertical planes, whose equators are on the xy-plane. The xy-plane represents all the infinity points in $\mathbb{H}^3$. The rigid motion in H^3 is determined by its restriction on the xy-plane, which is a Möbius transformation on the plane, in the form

$$\frac{az + b}{cz + d}, ac - bd = 1, a, b, c, d \in \mathbb{C}.$$

Most of the computation is carried out on the xy-plane.

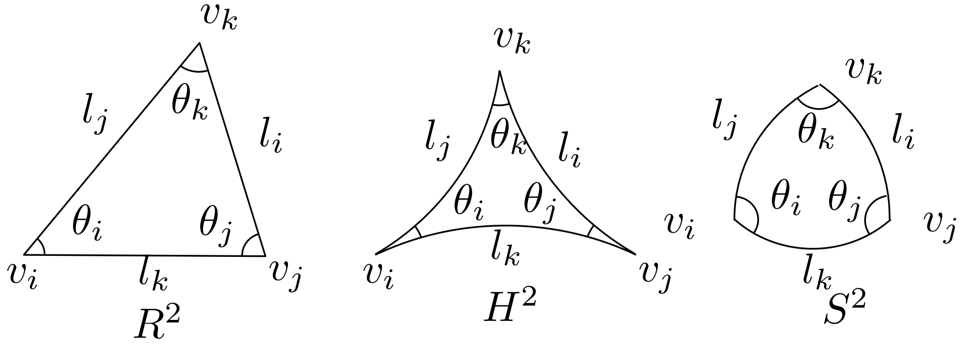

Fig. 3. Euclidean, hyperbolic and Spherical triangles.

As shown in figure 4, triangles with spherical , Euclidean or hyperbolic background geometry (meaning triangles in $\mathbb{S}^2$, $\mathbb{E}^2$ and $\mathbb{H}^2$) satisfy different cosine laws:

$$\left(\mathbb{S}^2\right) \quad \cos l_i = \frac{\cos\theta_i + \cos\theta_j \cos\theta_k}{\sin\theta_j \sin\theta_k} \tag{5}$$

$$\left(\mathbb{H}^2\right) \quad \cosh l_i = \frac{\cos\theta_i + \cos\theta_j \cos\theta_k}{\sin\theta_j \sin\theta_k} \tag{6}$$

$$\left(\mathbb{E}^2\right) \quad 1 = \frac{\cos\theta_i + \cos\theta_j \cos\theta_k}{\sin\theta_j \sin\theta_k} \tag{7}$$

We can interchange the role of edge and angle and get another three cosine laws:

$$\left(\mathbb{S}^2\right) \quad \cos\theta_i = \frac{\cos l_i - \cos l_j \cos l_k}{\sin l_j \sin l_k} \tag{8}$$

$$\left(\mathbb{H}^2\right) \quad \cos\theta_i = \frac{-\cosh l_i + \cosh l_j \cosh l_k}{\sinh l_j \sinh l_k} \tag{9}$$

$$\left(\mathbb{E}^2\right) \quad \cos\theta_i = \frac{-l_i^2 + l_j^2 + l_k^2}{2 l_j l_k} \tag{10}$$

For the right-angled hyperbolic hexagon, let l_1, l_2, l_3 be three non-pairwise adjacent edges of the hexagon and the opposite edges $\theta_1, \theta_2, \theta_3$, the cosine law is

$$\left(\mathbb{H}^2\right) \quad \cosh l_i = \frac{\cosh\theta_i + \cosh\theta_j \cosh\theta_k}{\sinh\theta_i \sinh\theta_k}. \tag{11}$$

Based on the cosine laws, curvature flows on smooth surfaces can be generalized to discrete cases.

2.6 The Smooth Surface Ricci Flow

Suppose S is a smooth surface with a Riemannian metric $\mathbf{g}$. The Ricci flow deforms the metric $\mathbf{g}(t)$ according to the Gaussian curvature $K(t)$ (induced by

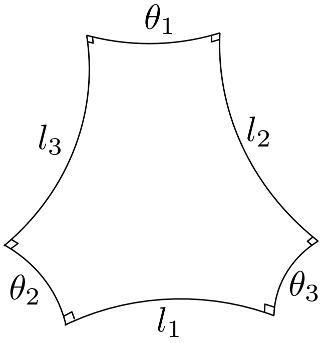

Fig. 4. Hyperbolic right-angled hexagon.

itself), where t is the time parameter

$$\frac{dg_{ij}(t)}{dt} = -2K(t)g_{ij}(t). \tag{12}$$

There is an analogy between the Ricci flow and the heat diffusion process. Suppose $T(t)$ is a temperature field on the surface. The heat diffusion equation is $dT(t)/dt = -\Delta_{\mathbf{g}}T(t)$, where $\Delta_{\mathbf{g}}$ is the Laplace-Beltrami operator induced by the surface metric. The temperature field becomes more and more uniform with the increase of t, and it will become constant eventually.

In a physical sense, the curvature evolution induced by the Ricci flow is exactly the same as heat diffusion on the surface, as follows:

$$\frac{dK(t)}{dt} = -\Delta_{\mathbf{g}(t)}K(t), \tag{13}$$

where $\Delta_{\mathbf{g}(t)}$ is the Laplace-Beltrami operator induced by the metric $\mathbf{g}(t)$. If we replace the metric in Eq. 12 with $g(t) = e^{2u(t)}g(0)$, then the Ricci flow can be simplified as

$$\frac{du(t)}{dt} = -2K(t), \tag{14}$$

which states that the metric should change according to the curvature.

The following theorems postulate that the Ricci flow defined in Eq. 12 is convergent and leads to a conformal uniformization metric. For surfaces with non-positive Euler numbers, Hamilton proved the convergence of the Ricci flow in [Ham88]:

Theorem 2 (Hamilton 1988). *For a closed surface of non-positive Euler characteristic, if the total area of the surface is preserved during the flow, the Ricci flow will converge to a metric such that the Gaussian curvature is constant everywhere.*

It is much more difficult to prove the convergence of the Ricci flow on surfaces with positive Euler numbers. The following result was proven by Chow in [Cho91]:

Theorem 3 (Chow 1991). *For a closed surface of positive Euler characteristic, if the total area of the surface is preserved during the flow, the Ricci flow will converge to a metric such that the Gaussian curvature is constant everywhere.*

The corresponding metric $\mathbf{g}(\infty)$ is the *uniformization metric.* Moreover, at any time t, the metric $\mathbf{g}(t)$ is conformal to the original metric $\mathbf{g}(0)$.

The Ricci flow can be easily modified to compute a metric with a *user-defined* curvature $\bar{K}$ as the following,

$$\frac{du(t)}{dt} = 2(\bar{K} - K). \tag{15}$$

With this modification, the solution metric $\mathbf{g}(\infty)$ can be computed, which induces the curvature $\bar{K}$.

3 Theories on The Discrete Surface Ricci Flow

In engineering fields, smooth surfaces are often approximated by simplicial complexes (triangle meshes). Major concepts, such as metric, curvature, and conformal deformation in the continuous setting can be generalized to the discrete setting. We denote a triangle mesh as Σ, a vertex set as V, an edge set as E, and a face set as F. e_{ij} represents the edge connecting vertices v_i and v_j, and f_{ijk} denotes the face formed by v_i, v_j, and v_k.

3.1 Background Geometry

In graphics, it is always assumed that a mesh Σ is embedded in the three dimensional Euclidean space $\mathbb{R}^3$, and therefore each face is Euclidean. In this case, we say the mesh is with Euclidean background geometry (see Fig. 2(a)). The angles and edge lengths of each face satisfy the Euclidean cosine law.

Similarly, if we assume that a mesh is embedded in the three dimensional sphere $\mathbb{S}^3$, then each face is a spherical triangle. We say the mesh is with spherical background geometry (see Fig. 2(b)). The angles and the edge lengths of each face satisfy the spherical cosine law.

Furthermore, if we assume that a mesh is embedded in the three dimensional hyperbolic space $\mathbb{H}^3$, then all faces are hyperbolic triangles. We say the mesh is with hyperbolic background geometry (see Fig. 2(c)). The angles and the edge lengths of each face satisfy the hyperbolic cosine law.

In the following discussion, we will explicitly specify the background geometry for a mesh when it is needed. Otherwise, the concept or the algorithm is appropriate for all kinds of background geometries.

3.2 Discrete Riemannian Metric

A discrete Riemannian metric on a mesh Σ is a piecewise constant metric with cone singularities. A metric on a mesh with Euclidean metric is a discrete Euclidean metric with cone singularities. Each vertex is a cone singularity. Similarly, a metric on a mesh with spherical background geometry is a discrete spherical metric with cone singularities; a metric on a mesh with hyperbolic background geometry is a discrete hyperbolic metric with cone singularities.

The edge lengths of a mesh Σ are sufficient to define a discrete Riemannian metric,

$$l : E \to \mathbb{R}^+, \tag{16}$$

as long as, for each face f_{ijk}, the edge lengths satisfy the triangle inequality: $l_{ij} + l_{jk} > l_{ki}$ for all the three background geometries, and another inequality: $l_{ij} + l_{jk} + l_{ki} < 2\pi$ for spherical geometry.

3.3 Discrete Gaussian Curvature

The discrete Gaussian curvature K_i on a vertex $v_i \in \Sigma$ can be computed from the angle deficit,

$$K_i = \begin{cases} 2\pi - \sum_{f_{ijk}\in F} \theta_i^{jk}, \, v_i \notin \partial\Sigma \\ \;\pi - \sum_{f_{ijk}\in F} \theta_i^{jk}, \, v_i \in \partial\Sigma \end{cases} \tag{17}$$

where θ_i^{jk} represents the corner angle attached to vertex v_i in the face f_{ijk}, and $\partial\Sigma$ represents the boundary of the mesh. The discrete Gaussian curvatures are determined by the discrete metrics.

3.4 Discrete Gauss-Bonnet Theorem

The Gauss-Bonnet theorem (Eq. 2) states that the total curvature is a topological invariant. It still holds on meshes as follows.

$$\sum_{v_i\in V} K_i + \lambda \sum_{f_i\in F} A_i = 2\pi\chi(M), \tag{18}$$

where A_i denotes the area of face f_i, and λ represents the constant curvature for the background geometry; $+1$ for the spherical geometry, 0 for the Euclidean geometry, and -1 for the hyperbolic geometry.

3.5 Discrete Conformal Deformation

Conformal metric deformations preserves infinitesimal circles and the intersection angles among them. The discrete conformal deformation of metrics uses circles with finite radii to approximate the infinitesimal circles.

The concept of the circle packing metric was introduced by Thurston in [Thu76] as shown in Fig. 5. Let Γ be a function defined on the vertices, $\Gamma : V \to \mathbb{R}^+$, which assigns a radius γ_i to the vertex v_i. Similarly, let Φ be a function defined on the edges, $\Phi : E \to [0, \frac{\pi}{2}]$, which assigns an acute angle $\Phi(e_{ij})$ to each edge e_{ij} and is called a *weight* function on the edges. Geometrically, $\Phi(e_{ij})$ is the intersection angle of two circles centered at v_i and v_j. The pair of vertex radius function and edge weight function on a mesh Σ, (Γ, Φ), is called a *circle packing metric* of Σ.

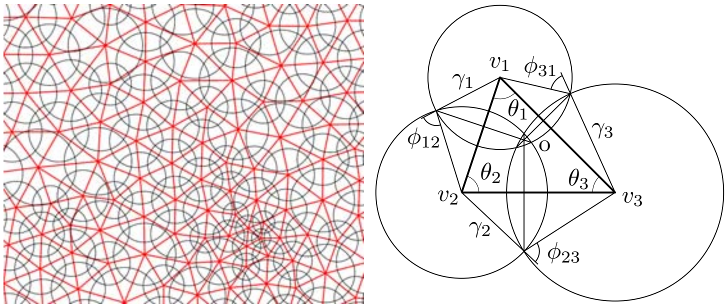

(a) (b)

Fig. 5. Circle Packing Metric (a) Flat circle packing metric (b) Circle packing metric on a triangle.

Fig. 5 illustrates the circle packing metrics. Each vertex v_i has a circle whose radius is γ_i. For each edge e_{ij}, the intersection angle ϕ_{ij} is defined by the two circles of v_i and v_j, which either intersect or are tangent.

Two circle packing metrics $(\mathit{\Gamma}_1, \mathit{\Phi}_1)$ and $(\mathit{\Gamma}_2, \mathit{\Phi}_2)$ on the same mesh are *conformally equivalent* if $\mathit{\Phi}_1 \equiv \mathit{\Phi}_2$. A *conformal deformation* of a circle packing metric only modifies the vertex radii and preserves the intersection angles $\mathit{\Phi}$ on the edges.

3.6 Admissible Curvature Space

A mesh $\mathit{\Sigma}$ with edge weight $\mathit{\Phi}$ is called a *weighted mesh*, which is denoted as $(\mathit{\Sigma}, \mathit{\Phi})$. In the following, we want to clarify the spaces of all possible circle packing metrics and all possible curvatures of a weighted mesh.

Let the vertex set be $V = \{v_1, v_2, \cdots, v_n\}$, and the radii be $\mathit{\Gamma} = \{\gamma_1, \gamma_2, \cdots, \gamma_n\}$. Let u_i be

$$u_i = \begin{cases} \log \gamma_i & \mathbb{E}^2 \\ \log \tanh \frac{\gamma_i}{2} & \mathbb{H}^2 \\ \log \tan \frac{\gamma_i}{2} & \mathbb{S}^2 \end{cases} \tag{19}$$

where $\mathbb{E}^2$, $\mathbb{H}^2$, and $\mathbb{S}^2$ indicate the background geometry of the mesh. We represent a circle packing metric on $(\mathit{\Sigma}, \mathit{\Phi})$ by a vector $\mathbf{u} = (u_1, u_2, \cdots, u_n)^T$. Similarly, we represent the Gaussian curvatures at mesh vertices by the curvature vector $\mathbf{k} = (K_1, K_2, \cdots, K_n)^T$. All the possible $\mathbf{u}$'s form the *admissible metric space*, and all the possible $\mathbf{k}$'s form the *admissible curvature space*.

According to the Gauss-Bonnet theory (Eq. 18), the total curvature must be $2\pi\chi(\mathit{\Sigma})$, and therefore the curvature space is $n-1$ dimensional. We add one linear constraint to the metric vector $\mathbf{u}$, $\sum u_i = 0$, for the normalized metric. As a result, the metric space is also $n-1$ dimensional. If all the intersection angles are acute, then the edge lengths induced by a circle packing satisfy the triangle inequality. There is no further constraint on $\mathbf{u}$. Therefore, the admissible metric space is simply $\mathbb{R}^{n-1}$.

A curvature vector $\mathbf{k}$ is *admissible* if there exists a metric vector $\mathbf{u}$, which induces $\mathbf{k}$. The admissible curvature space of a weighted mesh (Σ, Φ) is a convex polytope, specified by the following theorem. The detailed proof can be found in [CL03].

Theorem 4. *Suppose (Σ, Φ) is a weighted mesh with Euclidean background geometry, I is a proper subset of vertices, F_I is the set of faces whose vertices are in I and the link set $Lk(I)$ is formed by faces (e, v), where e is an edge and v is the third vertex in the face,*

$$Lk(I) = \{(e, v) | e \cap I = \emptyset, v \in I\},$$

then a curvature vector $\mathbf{k}$ is admissible if and only if

$$\sum_{v_i \in I} K_i > - \sum_{(e,v) \in Lk(I)} (\pi - \phi(e)) + 2\pi\chi(F_I). \tag{20}$$

The admissible curvature space for weighted meshes with hyperbolic or spherical background geometries is more complicated. We refer the readers to [LGD07] for detailed discussion.

3.7 The Discrete Surface Ricci Flow

Suppose (Σ, Φ) is a weighted mesh with an initial circle packing metric. The discrete Ricci flow is defined as follows.

$$\frac{du_i(t)}{dt} = (\bar{K}_i - K_i), \tag{21}$$

where $\bar{\mathbf{k}} = (\bar{K}_1, \bar{K}_2, \cdots, \bar{K}_n)^T$ is the user defined target curvature. The discrete Ricci flow has exactly the same form as the smooth Ricci flow (Eq. 15), which deforms the circle packing metric according to the Gaussian curvature, as in Eq. 21.

The discrete Ricci flow can be formulated in the variational setting, namely, it is a negative gradient flow of a special energy form. Let (Σ, Φ) be a weighted mesh with spherical (Euclidean or hyperbolic) background geometry. For two arbitrary vertices v_i and v_j, the following symmetric relation holds:

$$\frac{\partial K_i}{\partial u_j} = \frac{\partial K_j}{\partial u_i}.$$

Let $\omega = \sum_{i=1}^n K_i du_i$ be a differential one-form [Wei07]. The symmetric relation guarantees that the one-form is closed (curl free) in the metric space.

$$d\omega = \sum_{i,j} (\frac{\partial K_i}{\partial u_j} - \frac{\partial K_j}{\partial u_i}) du_i \wedge du_j = 0.$$

By Stokes theorem, the following integration is path independent,

$$f(\mathbf{u}) = \int_{\mathbf{u_0}}^{\mathbf{u}} \sum_{i=1}^{n} (\bar{K}_i - K_i) du_i, \tag{22}$$

where $\mathbf{u_0}$ is an arbitrary initial metric. Therefore, the above integration is well defined, and is called the *discrete Ricci energy.* The discrete Ricci flow is the negative gradient flow of the discrete Ricci energy. The discrete metric which induces $\bar{\mathbf{k}}$ is the minimizer of the energy.

Computing the desired metric with user-defined curvature $\bar{\mathbf{k}}$ is equivalent to minimizing the discrete Ricci energy.For Euclidean or hyperbolic cases, the discrete Ricci energy (see Eq. 22) was first proved to be strictly convex in the seminal work of Colin de Verdiere [dVY91] for the $\Phi = 0$ case, and was generalized to all cases of $\Phi \leq \pi/2$ in [CL03]. The global minimum uniquely exists, corresponding to the metric $\bar{\mathbf{u}}$, which induces $\bar{\mathbf{k}}$. The discrete Ricci flow converges to this global minimum.

Theorem 5 (Chow & Luo: Euclidean Ricci Energy). *The Euclidean Ricci energy $f(\mathbf{u})$ on the space of the normalized metric $\sum u_i = 0$ is strictly convex.*

Theorem 6 (Chow & Luo: Hyperbolic Ricci Energy). *The hyperbolic Ricci energy is strictly convex.*

Although the spherical Ricci energy is not strictly convex, the desired metric $\bar{\mathbf{u}}$ is still a critical point of the energy. In our experiments, the solution can be reached using Newton's method.

4 Algorithm of The Discrete Surface Ricci Flow

In this section, we explain the algorithm in detail. The unified pipeline for all kinds of the discrete Ricci flow algorithms is as follows:
1. Determine the target curvature and the background geometry;
2. Compute the initial circle packing metric;
3. Optimize the Ricci energy using either gradient descent or Newton's methods;
4. Compute the layout using the result metric.

Step 1. Determine the Target Curvature and the Background Geometry

The user is free to define the target curvatures for different applications, while obeying the Gauss-Bonnet theorem in Eq. 18 and admissible condition in Eq. 20.

For example, for constructing manifold splines (see [GHQ06] for details), it is desirable to obtain a flat metric with a minimal number of cone singularities. One can concentrate all the curvatures at a single vertex and make everywhere else flat. In this case, the background geometry of the mesh is chosen to be Euclidean and the curvature for the selected vertex is set to $2\pi\chi(\Sigma)$. The curvature at all other vertices is set to zero.

For the application of surface classification using conformal structures (see [JLYG07] for details), no cone singularities are allowed. All of the curvatures must be evenly distributed over the whole surface. In this case, the target curvature is zero for all vertices and the background geometry is hyperbolic for high genus meshes.

Step 2. Compute the Initial Circle Packing Metric

In this step, the initial circle packing metric (Γ, Φ) is computed. This metric should approximate the original Euclidean metric as much as possible. Suppose d_{ij} is the length of edge e_{ij} determined by the induced Euclidean metric in $\mathbb{R}^3$, l_{ij} is the edge length determined by the circle packing metric. Let ϕ_{ij} be the edge weight, γ_i and γ_j be the circle radii on vertices v_i and v_j, then l_{ij} can be computed according to the cosine law with different background geometries:

$$\begin{aligned} l_{ij}^2 &= \gamma_i^2 + \gamma_j^2 + 2\gamma_i\gamma_j \cos\phi_{ij}, & \mathbb{E}^2 \\ \cosh l_{ij} &= \cosh\gamma_i \cosh\gamma_j + \sinh\gamma_i \sinh\gamma_j \cos\phi_{ij}, & \mathbb{H}^2 \\ \cos l_{ij} &= \cos\gamma_i \cos\gamma_j - \sin\gamma_i \sin\gamma_j \cos\phi_{ij}, & \mathbb{S}^2 \end{aligned} \tag{23}$$

The initial circle packing metric can be obtained by minimizing the following energy

$$\min_{\gamma_i, \phi_{ij}} \sum_{e_{ij} \in \Sigma} |d_{ij} - l_{ij}|^2,$$

such that $\phi_{ij} \in (0, \frac{\Pi}{2}]$. If the initial mesh has too many obtuse angles and the requirement for the conformality is very high, we can use an extra re-meshing step to improve the triangulation quality.

Step 3. Optimize The Ricci Energy

In the following we introduce two methods to optimize the Ricci energy; one is the gradient descent method and the other is Newton's method.

Gradient Descent

The Ricci energy can be optimized using the gradient descent method, which is the direct analogy of the smooth Ricci flow. Note that during the computation the vertex radii Γ vary over time while the edge weights Φ are fixed. This reflects the fact that conformal metric deformation preserves angles.

1.Compute edge lengthes l_{ij} from the current vertices radii γ_i and γ_j and the fixed edge weight ϕ_{ij}, using the cosine law (Eq. 23) for the background geometry.

2.Compute the corner angles θ_i^{jk} in each face f_{ijk} from the current edge lengths by using the cosine law according to the background geometry.

3.Compute the discrete Gaussian curvature K_i of each vertex v_i by using Eq. 17.

4.Update u_i of each vertex v_i by using Eq. 22, as follows.

$$u_i = u_i + \epsilon(\bar{K}_i - K_i),$$

where $\bar{K}_i$ is the target Gaussian curvature. In our experiments, ϵ is no greater than 0.05.

5. Normalize the metrics. Let $s = \sum u_i$, then $u_i = u_i - \frac{s}{n}$, where n is the total number of vertices.

6. Update the radius γ_i of each vertex v_i, using u_i and Eq. 19.

7. Repeat the steps from 1 through 5, until the maximal curvature error falls below a threshold, $\max |\bar{K}_i - K_i| < \delta$, where δ is a user-specified error tolerance.

Newton's Method

As described in Section 3.6, the Ricci flow is the negative gradient flow of the discrete Ricci energy in Eq. 22. We can further improve the convergence speed by using Newton's method.

The key to Newton's method is to compute the Hessian matrix. Different Ricci flows have different Hessian matrices according to their background geometries. The Hessian matrix for the Euclidean Ricci energy is explained here. We refer readers to [JKLG08] for other cases.

As shown in figure 5, for each face, there are three circles centered at its vertices. Then there exists a unique circle, which is orthogonal to all three circles, whose center is called the center of the face. Two circles centered at the end vertices of an edge share a common chord. Three common chords intersect at the center o as shown in the figure. The center can be calculated explicitly. Let e_{ij} be an edge, attaching to two faces f_1 and f_2, whose centers are o_1 and o_2. The distance from o_k to e_{ij} is h_k, $k = 1, 2$. The edge coefficient w_{ij} is defined as

$$w_{ij} = h_1 + h_2.$$

If e_{ij} is on the boundary, f_2 does not exist, then $w_{ij} = h_1$.

The elements in the Hessian matrix are $\partial K_i/\partial u_j$, which has the following explicit formula

$$\frac{\partial K_i}{\partial u_j} = \begin{cases} -w_{ij} & i \neq j \\ \sum_k w_{ik} & i = j \end{cases}$$

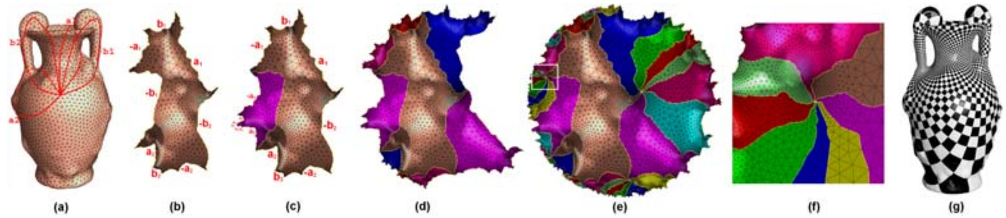

Fig. 6. The hyperbolic Ricci flow (a) Genus two vase model marked with a set of canonical fundamental group generators which cut the surface into a topological disk with eight sides: a_1, b_1, a_1^{-1}, b_1^{-1}, a_2, b_2, a_2^{-1}, b_2^{-1}. (b) The fundamental domain is conformally flattened onto the Poincaré disk with marked sides. (c) A Möbius transformation moves the side b_1 to b_1^{-1}. (d) Eight copies of the fundamental domain are glued coherently by eight Möbius transformations. (e) A finite portion of the universal covering space is flattened onto the Poincaré disk. (f) Zoom in on a region on the universal covering space, where eight fundamental domains join together. No seams or overlapping can be found. (g) Conformal parameterization induced by the hyperbolic flattening. The corners angle of checkers are well-preserved.

Step 4. Compute the Layouts

In this step, we flatten the mesh with the target metric onto one of the canonical domains: the plane $\mathbb{E}^2$, the sphere $\mathbb{S}^2$, or the hyperbolic space $\mathbb{H}^2$. The algorithms in this step involve several topological concepts, such as fundamental domain,

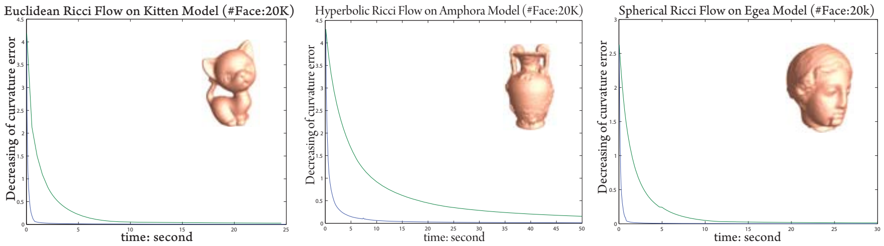

(a) Euclidean (b) Hyperbolic (c) Spherical

Fig. 7. Performance of the Ricci flow The horizontal axis represents time, and the vertical axis represents the maximal curvature error. The blue curves are for the Newton's method; the green curves are for the gradient descent method. The meshes have about $30k$ faces. The tests were carried out on a laptop with 1.7GHz CPU and 1G RAM. All the algorithms are written in C++ on a Windows platform without using any other numerical library.

canonical fundamental group basis, universal covering space, etc. The following is the unified pipeline for computing the layout:
1. Flatten a seed face.
2. Flatten a fundamental domain.
3. Flatten the universal covering space.
In the following, we focus on hyperbolic case only. The other two cases are very similar, details can be found in [JKLG08].

1.Flatten a Seed Face

We randomly select a seed face f_{012}, and compute the parametric positions of the vertices v_0, v_1, and v_2 using the edge lengths of f_{012}. In the hyperbolic case, the positions are set as $\tau(v_0) = (0,0)$:

$$\tau(v_1) = \frac{e^{l_{01}}-1}{e^{l_{01}}+1}(1,0), \tau(v_2) = \frac{e^{l_{02}}-1}{e^{l_{02}}+1}(\cos\theta_0^{12}, \sin\theta_0^{12});$$

Then we put faces adjacent to the seed face into a queue.

2. Flatten a Fundamental Domain

In this step, we propagate the flattening to the rest of all faces, namely we want to embed a fundamental domain. We call the resulting layout a *fundamental polygon*.

To propagate the flattening, we put all unprocessed faces adjacent to the current face into the queue. We pop a face f_{ijk} from the queue and test whether all its vertices have been set to parametric positions. If so, we continue to pop the next one from the queue as long as the queue is nonempty. Otherwise, suppose that v_i and v_j have been embedded, then $\tau(v_k)$ can be computed as one of the two intersection points between the two circles, $c(\tau(v_i), l_{ki})$ and $c(\tau(v_j), l_{kj})$, satisfying $(\tau(v_j)-\tau(v_i)) \times (\tau(v_k)-\tau(v_i)) > 0$. computing the intersection points between hyperbolic circles boils down to finding intersections between Euclidean circles.

Different choices of the seed faces induce different layouts, which differ by a rigid motion. In the hyperbolic case, it is a Möbius transformation. Fig. 6 (b), (c) and (d) are the layouts for the same genus two model, shown in Fig. 6 (a), with different seed faces marked in red. The layouts in (c) and (d) are transformed to align with the layout in (b) by different Möbius transformations, as shown in Fig. 6(e).

3 Flatten the Universal Covering Space

For the purpose of texture mapping, it is enough to flatten a fundamental domain. For the purpose of constructing a manifold spline (see [GHQ06] for details) or surface classification by conformal equivalence (see [JLYG07] for details), we need to flatten a finite portion of the universal covering space.

The universal covering space of a mesh with a negative Euler number can be embedded onto the whole hyperbolic space $\mathbb{H}^2$. The algorithmic pipeline is as follows:
1. Embed a canonical fundamental domain.
2. Compute the deck transformation group generators.
3. Tile the whole canonical domain $\mathbb{R}^2$ or $\mathbb{H}^2$.

In the first step, we find a canonical fundamental group basis, then generate a canonical fundamental domain, then we flatten this canonical fundamental domain.

Figure 6(b) gives the embedding of the canonical fundamental domain for genus two amphora model on the Poincaré disk.

Compute Deck Transformation Group Generators

The embedding of a canonical fundamental domain for a closed genus g surface has $4g$ different sides, which induce $2g$ rigid transformations (as explained in below). These $2g$ rigid motions are the generators of the deck transformation group.

Fig. 6 illustrates the process for a mesh with a negative Euler number. Let $\{a_1, b_1, \cdots, a_g, b_g\}$ be a set of canonical fundamental group generators, where g is the genus. The embedding of its canonical fundamental domain in hyperbolic space has $4g$ sides, $\tau(a_1), \tau(b_1), \tau(a_1^{-1}), \tau(b_1^{-1}), ..., \tau(a_g), \tau(b_g), \tau(a_g^{-1}), \tau(b_g^{-1})$ (see Fig. 6(b) in Poincaré disk). There exists unique Möbius transformations α_k, β_k, which map the $\tau(a_k)$ and $\tau(b_k)$ to $\tau(a_k^{-1})$ and $\rho(b_k^{-1})$ respectively, as shown in Fig. 6(c) and (d). The Möbius transformations $\{\alpha_1, \beta_1, \alpha_2, \beta_2, \cdots, \alpha_g, \beta_g\}$ form a set of generators of the deck transformation group.

Tile the Canonical Domain

Any deck transformation can be produced by composing the generators $\{\alpha_k, \beta_k\}$. Then the whole canonical domain can be tiled by transforming a fundamental polygon by all deck transformations. This induces a flattening of the universal covering space of the mesh onto the canonical domain. Fig. 6(e) illustrates the layout of the universal covering space of a genus two amphora model onto the whole Poincaré disk.

The computation of the layout for a genus one surface is very similar, Fig. 8 shows the whole process for the kitten model.

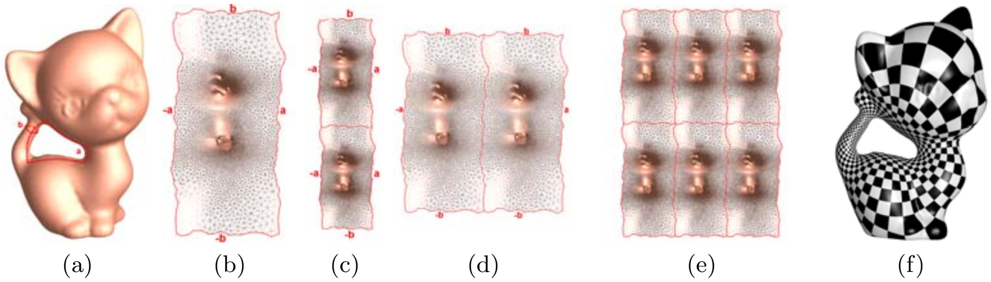

(a) (b) (c) (d) (e) (f)

Fig. 8. The Euclidean Ricci flow (a) Genus one kitten model marked with a set of canonical fundamental group generators a and b. (b) A fundamental domain is conformally flattened onto the plane, marked with four sides $aba^{-1}b^{-1}$. (c) One translation moves the side b to b^{-1}. (d) The other translation moves the side a to a^{-1}. (e) The layout of the universal covering space of the kitten mesh on the plane, which tiles the plane. (f) The conformal parameterization is used for the texture mapping purpose. A checkerboard texture is placed over the parameterization in b). The conformality can be verified from the fact that all the corner angles of the checkers are preserved.

5 Discrete Surface Yamabe Flow

For smooth surfaces, the Ricci flow and Yamabe flow are equivalent. In discrete case, there is subtle difference, which is caused by a different notion of discrete conformal classes. The following summarizes the sharp distinctions:

1. The discrete Ricci flow requires circle packing, whereas discrete Yamabe flow is directly defined on triangulations. Therefore, Yamabe flow is more flexible.
2. Both the Ricci flow and the Yamabe flow are variational. The energy form for the Ricci flow and the Yamabe flow are convex. But the metric space (domain of $\mathbf{u}$) of the Ricci flow is convex, while the metric space of Yamabe flow is non-convex. Therefore, it is stable to use Newton's method for optimizing the Ricci energy. For Yamabe energy optimization, the algorithm takes more caution.
3. Yamabe flow can adapt the connectivity to the target curvature automatically, which makes it valuable for practical purposes. During Yamabe flow, if the algorithm detects a degenerate triangle, where one angle becomes π, then the algorithm swaps the edge against the angle and continue the flow. Unfortunately, this important technique of adapting connectivity to the target curvature during the flow can not be generalized to the Ricci flow directly.

Using the symbols in the previous discussion, let M be a triangle mesh embedded in $\mathbb{R}^3$. Let e_{ij} be an edge with end vertices v_i and v_j. d_{ij} is the edge length of e_{ij} induced by the Euclidean metric of $\mathbb{R}^3$. A function defined on the vertices $\mathbf{u} : V \to \mathbb{R}$ is the *discrete conformal factor*. The edge length l_{ij} is defined as

$$l_{ij} = e^{u_i + u_j} d_{ij}. \tag{24}$$

Let K_i and $\bar{K}_i$ denote the current vertex curvature and the target vertex curvature respectively. The discrete Yamabe flow is defined as

$$\frac{du_i(t)}{dt} = \bar{K}_i - K_i, \tag{25}$$

with initial condition $u_i(0) = 0$. The convergence of Yamabe flow is proven in [Luo04]. Furthermore, Yamabe flow is the gradient flow of the following Yamabe energy, let $\mathbf{u} = (u_1, u_2, \cdots, u_n)$,$n$ is the total number of vertices,

$$f(\mathbf{u}) = \int_{\mathbf{u}_0}^{\mathbf{u}} \sum_i^n (\bar{K}_i - K_i) du_i. \tag{26}$$

Similar to the Ricci flow, one can show that

$$\frac{\partial K_i}{\partial u_j} = \frac{\partial K_j}{\partial u_i} \tag{27}$$

The Yamabe energy is well defined and convex. The Hessian matrix can be easily constructed as follows. Suppose faces f_{ijk} and f_{jil} are adjacent to the edge e_{ij}, define the *weight* of the edge e_{ij} as

$$w_{ij} = \cot\theta_k + \cot\theta_l, \tag{28}$$

where θ_k is the angle at v_k in f_{ijk}, θ_l is the angle at v_l in face f_{jil}. If the edge is on the boundary, and only attaches to f_{ijk}, then

$$w_{ij} = \cot\theta_k.$$

It can be shown by direct computation, the differential relation between the curvature and the conformal factor is

$$dK_i = \sum_j w_{ij}(du_i - du_j). \tag{29}$$

So the Hessian matrix of the yamabe energy is given by

$$\frac{\partial^2 f(\mathbf{u})}{\partial u_i \partial u_j} = -\frac{\partial K_i}{\partial u_j} = \begin{cases} w_{ij} & , i \neq j \\ -\sum_k w_{ik} & , i = j \end{cases} \tag{30}$$

The Hessian matrix is positive definite on the linear subspace $\sum_i u_i = 0$. By using the Hessian matrix formulate 30, the Yamabe energy 26 can be optimized effectively. But the major difficulty is that the *admissible metric space* $\Omega(\mathbf{u})$ for a mesh with fixed connectivity is not convex,

$$\Omega(\mathbf{u}) = \{\mathbf{u} | \forall f_{ijk} \in M, l_{ij} + l_{jl} > l_{li}\}$$

Therefore, during the optimization process using Newton's method, we need to ensure that the metric $\mathbf{u}$ is in the admissible metric space $\Omega(u)$ at each step. If

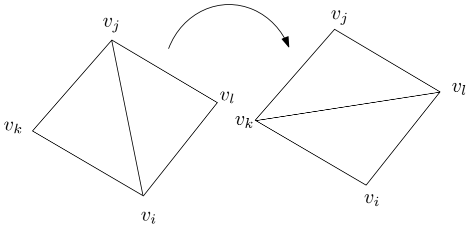

Fig. 9. Edge swap

a degenerated triangle f_{ijk} is detected, then we swap the longest edge of it. For example, if θ_k exceeds π, then we swap edge e_{ij} as shown in figure 9. The major difficulty for the discrete Ricci flow is to find a good initial circle packing with all acute edge intersection angles. This problem does not exist for discrete Yamabe flow. Therefore, yamabe flow in general produces better conformality in practice. Figure 10 shows the conformal parameterizations using Yamabe flow. In frames (a) and (b), the boundary target curvature is $\frac{2\pi}{m}$, where m is the total number of boundary vertices. In frames (c) and (d), the curvatures at the four corners are $\frac{\pi}{2}$'s, and are zeros everywhere else. The number of edge swaps depends on the initial connectivity, initial curvatures and the target curvatures.

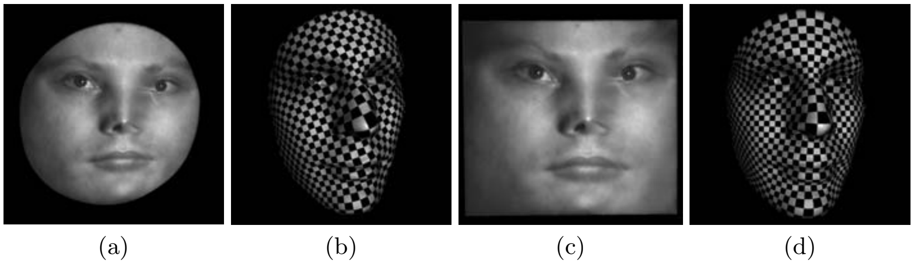

Fig. 10. Conformal parameterizations using Yamabe flow. (a) and (b), the boundary curvature is constant. (c) and (d), the curvatures at the four corners are $\frac{\pi}{2}$, and are zeros everywhere else.

There are many variations for discrete surface curvature flow. In the following, we discuss two of them: out-of-core mesh curvature flow, and curvature flow under mixed constraints.

Out-of-Core Curvature Flow In practice, if the input mesh is too big to be contained in the memory of the computer, we call it a *out-of-core mesh.* The following method can be used to compute the desired metric for an out-of-core mesh based on either the Ricci flow or Yamabe flow. First, partition the vertex set V to $V_1, V_2, \cdots, V_k$, with each set being small enough to fit in the memory. We require that $V = \cup_{i=1}^{k} V_i$, and each vertex in V should be contained as inner vertex in at least one set V_l. Then the energy can be defined for each set

$$f_i(\mathbf{u}) = \int_{\mathbf{u}_0}^{\mathbf{u}} \sum_{v_j \in V_i} (\bar{K}_j - K_j) du_j.$$

Each $f_i(\mathbf{u})$ can be optimized separately and alternatively. Since the energy is convex, the alternating optimization converges to the global minima, which gives the desired metric.

Curvature Flow under Mixed Constraints Rather than specifying the target curvature for each vertex, we can specify target curvatures $\bar{K}_i$ for some vertices, and specify conformal factor $\bar{u}_j$ for the rest. Let $V = V_k \cup V_u$, $V_k \cap V_u = \emptyset$, for each $v_i \in V_k$, the target curvature $\bar{K}_i$ is given, for each $v_j \in V_u$, the target conformal factor $\bar{u}_j$ is given. By optimizing the following energy

$$f(\mathbf{u}) = \int_{\mathbf{u}_0}^{\mathbf{u}} \sum_{v_i \in V_k} (\bar{K}_i - K_i) du_i,$$

under the constraints

$$u_j = \bar{u}_j, \forall v_j \in V_u$$
$$K_i = \bar{K}_i, \forall v_i \in V_k$$

we can still get the unique solution, as long as the target curvatures and the target conformal factors are compatible.

6 Theories on Discrete Curvature Flow for 3-Manifolds

All surfaces admit metrics with constant Gaussian curvature. This fact essentially holds for 3-manifolds. According to the Poincaré conjecture and the Thurston's geometrization conjecture, all 3-manifolds can be canonically decomposed to prime 3-manifolds. All prime 3-manifolds can be further decomposed by tori into pieces so that each piece has one of eight canonical geometries.

The study of topological and geometric structures of three dimensional manifolds has fundamental impacts in science and engineering. Computational algorithms for 3-manifolds can help topologist and geometers to investigate the complicated structures of 3-manifolds. They also have great potentials for a wide range of applications in the engineering world. The most direct applications include volumetric parameterizations, volumetric shape analysis, volumetric deformation, solid modeling and etc. Figure 11 shows a simple example of the volumetric parameterization for the volumetric Max Planck model, which is a topological ball.

Similar to the surface case, most 3-manifolds admit hyperbolic metric, which has constant sectional curvature. A hyperbolic 3-manifolds with boundaries is shown in Fig. 12, where the 3-manifold is the 3-ball with a knotted pipe removed, which is called *Thurston's knotted Y-shape*. Hyperbolic 3-manifolds with

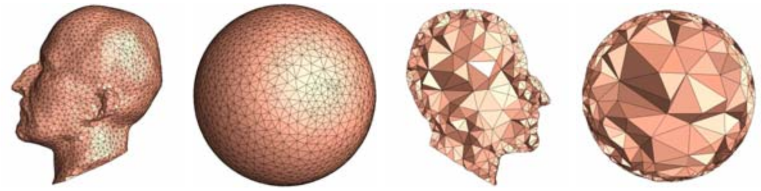

Fig. 11. Volumetric parameterization for a topological ball.

geodesic boundaries have the following topological properties:
1. The genus of boundary surfaces are greater than one.
2. For any closed curve on the boundary surface, if it can not shrink to a point on the boundary, then it can not shrink to a point inside the volume.

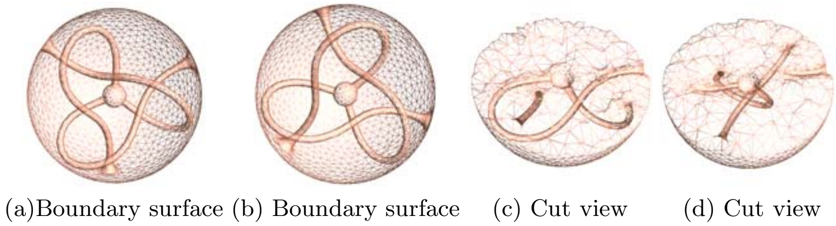

(a)Boundary surface (b) Boundary surface (c) Cut view (d) Cut view

Fig. 12. Thurston's Knotted Y-Shape.

Compared to the surface curvature flow, the discrete 3-dimensional curvature flow has some similar properties; meanwhile, it also owns some unique properties. Table 1 summaries the corresponding concepts involved in the curvature flow for surfaces and 3-manifolds respectively. For example, the primitive building blocks for surfaces are right-angled hyperbolic hexagons (Fig.13(c)); while for 3-manifolds, it is truncated hyperbolic tetrahedra (Fig.14). The discrete curvature used in the surface case is the vertex curvature (Fig.15), while for 3-manifolds it is the edge curvature (Fig. 16). The parameter domain for the surface case is the hyperbolic space $\mathbb{H}^2$ using the upper half plane model; the domain for 3-manifold case is the hyperbolic space $\mathbb{H}^3$ using the upper half space model. In the following part, we will address the similarities and differences in details respectively.

6.1 Similarities between Surface and Volumetric Curvature Flow

There are many intrinsic similarities between surface curvature flow and volumetric curvature flow. Discrete surface curvature flow can be naturally generalized to

3-manifold case. In particular, we have generalized the discrete hyperbolic Ricci flow from surfaces to 3-manifolds with geodesic boundaries. The 3-manifold is approximated by tetrahedra with hyperbolic background geometry, and the edge lengths determine the metric. During the curvature flow, the edge lengths are deformed according to the curvature. The resulting metric at the steady state will have the constant sectional curvature.

For the purpose of comparison, we first illustrate the discrete hyperbolic Ricci flow for surface case using figure 13. A surface with negative Euler number is parameterized and conformally embedded in the hyperbolic space $\mathbb{H}^2$. The three boundaries are mapped to geodesics. Given two arbitrary boundaries, there exists a unique geodesic orthogonal to both boundaries. Three such geodesics partition the whole surface into two right-angled hexagons, as shown in (c). A finite portion of the universal covering space is embedded in $\mathbb{H}^2$, as shown in(d).

For hyperbolic 3-manifolds with boundaries, things are quite similar. Given such a 3-manifold, such as the Thurston's knotted Y-shape in figure 12, discrete curvature flow can lead to the canonical hyperbolic metric. The boundary surface become hyperbolic planes, which are geodesic submanifolds. By finding certain hyperbolic planes orthogonal to the boundary surfaces, we can decompose the 3-manifold into several hyperbolic truncated tetrahedra, as shown in Fig.14. Using the canonical hyperbolic metric, a finite portion of the universal covering space can be embedded in $\mathbb{H}^3$, as shown in Fig.25.

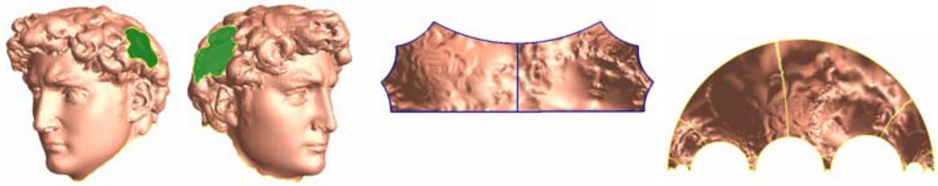

(a)Left view (b) Right view (c) Fundamental domain (d) Periodic embedding

Fig. 13. Surface with boundaries with negative Euler number can be conformally periodically mapped to the hyperbolic space $\mathbb{H}^2$.

	Surface	3-Manifold
Manifold	with negative Euler number with boundaries Fig.13	Hyperbolic 3-manifold with geodesic boundaries Fig.12
Building Block	hyperbolic right-angled hexagons Fig.13	Truncated hyperbolic tetrahedra Fig.14
Curvature	Gaussian curvature Fig 15	Sectional curvature Fig.15, Fig.16
Algorithm	Discrete Ricci flow	Discrete curvature flow
Parameter domain	Upper half plane $\mathbb{H}^2$ Fig.13	Upper half space $\mathbb{H}^3$ Fig.25

Table 1. Correspondence between surface and 3-manifold parameterizations.

6.2 Differences between Surface and 3-Manifold Curvature Flow

Although curvature flow presents many similarities for the surface case and 3-manifold case, there are yet fundamental differences between them. One of the most prominent differences is the so called *Mostow rigidity* [Mos68]. Mostow rigidity states that the geometry of a finite volume hyperbolic manifold (for dimension greater than two) is determined by the fundamental group. Namely, for two complete finite volume hyperbolic n-manifolds ($n > 2$) M and N, if there exists a topological isomorphism $f : \pi_1(M) \to \pi_1(N)$, it will induce a unique isometry from M to N. For the surface case, however, the geometry cannot be determined by the fundamental group. Suppose M and N are two surfaces with hyperbolic metrics; even if M and N share the same topology (i.e. there exists an isomorphisms $f : \pi_1(M) \to \pi_1(N)$), there may not exist an isometry from M to N. In another word, fixing the fundamental group of the surface M, there are infinitely many pairwise non-isometric hyperbolic metrics on M; each of them corresponds to a certain conformal structure of M.

In a nutshell, surfaces have conformal geometry, while 3-manifolds do not. All the Riemannian metrics on a topological surface S can be classified by conformal equivalence, each equivalence class is a *conformal structure.* If the surface is with a negative Euler number, then there exists a unique hyperbolic metric in each conformal structure.

As a consequence of Mostow rigidity, the conformality for 3-manifold parameterization is quite different from surface parameterization. Conformal surface parameterization is equivalent to find a metric with constant Gaussian curvature conformal to the induced Euclidean metric; that is, it requires the original induced Euclidean metric. Namely, the vertex positions or the edge lengths are essential parts of the input. In contrast, for 3-manifolds, only topological information is required. Different 3-manifolds have the same conformal parameterization if they have the same fundamental group. Consequently, the tessellation will affect the conformality of the surface parameterization, while it does not affect the computational results of 3-manifolds parameterization. Utilizing this special property, we can reduce the computational complexity of 3-manifold curvature flow by using the simplest triangulation for a given 3-manifold. For example, Thurston's Knotted Y-Shape in Fig.12 can be either represented as a high resolution tetrahedral mesh or a mesh with only 2 truncated tetrahedra, and the resulting canonical metrics are identical.

Besides the Mostow rigidity, there are some other unique properties of 3-manifold curvature flow, such as the representation of discrete curvature. On discrete surfaces, there are only vertex curvatures, which is measured as the angle deficient at each vertex. For discrete 3-manifolds (e.g. tetrahedral mesh), however, there are both vertex curvatures and edge curvatures. The vertex curvature equals to 4π minus all the surrounding solid angles; the edge curvature equals to 2π minus all the surrounding dihedral angles. And it turns out that the vertex curvatures are totally determined by the edge curvatures. In our algorithm, we use the edge curvature to drive the flow.

6.3 Theories on Discrete Curvature Flow for Hyperbolic 3-Manifolds

In this section, we introduce the theoretical foundations of discrete curvature flow for the class of 3-manifolds whose boundary is consisting of high genus surfaces. In particular, we will cover the discrete approximation of 3-manifolds, the representation of discrete curvature, and the principles of discrete curvature flow.

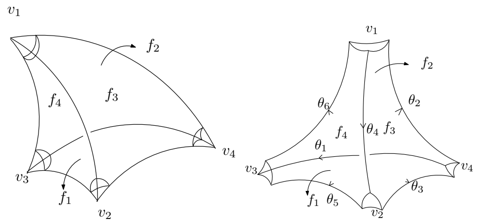

Fig. 14. Hyperbolic tetrahedron and truncated tetrahedron.

Hyperbolic Tetrahedron and Truncated Hyperbolic Tetrahedron 2-manifolds (surfaces) can be approximated by triangular meshes with different background geometries. Similarly, 3-manifolds can be approximated by tetrahedron meshes with different background geometry.

A closed 3-manifold can be triangulated using tetrahedra. The left frame in Fig.14 shows a hyperbolic tetrahedron $[v_1 v_2 v_3 v_4]$. Each face f_i of a hyperbolic tetrahedron is a hyperbolic plane, each edge e_{ij} is a hyperbolic line segment.

A 3-manifold with boundary can be tessellated using truncated tetrahedra. The right frame in Fig.14 shows a truncated hyperbolic tetrahedron, where the four vertices are truncated by hyperbolic planes. The cutting plane at vertex v_i is perpendicular to the edges e_{ij}, e_{ik}, e_{il}. Therefore, each face of a truncated hyperbolic tetrahedron is a right-angled hyperbolic hexagon, each cutting section is a hyperbolic triangle. If the given manifold is tessellated by multiple tetrahedra, the face hexagons will be glued one another, while the cutting triangles form the boundary surface.

The geometry of the truncated tetrahedron is determined by dihedral angles, represented as $\{\theta_1, \theta_2, \cdots, \theta_6\}$ in Fig.14. For example, the hyperbolic triangle at v_2 has inner angles $\theta_3, \theta_4, \theta_5$, its edge lengths can be determined using formula 7. For face f_4, the edge length e_{12}, e_{23}, e_{31} are determined by the hyperbolic triangles at v_1, v_2, v_3 using the right-angled hyperbolic hexagon cosine law 11.

For another point of view, the geometry of a truncated tetrahedron is reflected by the length of edges $e_{12}, e_{13}, e_{14}, e_{23}, e_{34}, e_{42}$. Due to the fact that each face is a right angled hexagon, the above six edge lengths will determine the edge lengths of each vertex triangle, and therefore determines its three inner angles, which equal to the corresponding dihedral angles.

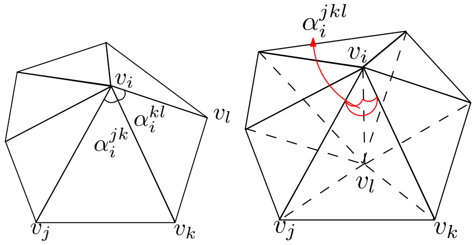

Fig. 15. Discrete vertex curvature for 2-manifold and 3-manifold.

Discrete Curvature For 3-manifolds, each tetrahedron $[v_i, v_j, v_k, v_l]$ (as shown in Fig.15) has four solid angles at their vertices, denoted as $\{\alpha_i^{jkl}, \alpha_j^{kli}, \alpha_k^{lij}, \alpha_l^{ijk}\}$. For an interior vertex, the vertex curvature is 4π minus the surrounding solid angles,

$$K(v_i) = 4\pi - \sum_{jkl} \alpha_i^{jkl}.$$

For a boundary vertex, the vertex curvature is 2π minus the surrounding solid angles.

Besides vertex curvature, the discrete approximation of a 3-manifold owns another type of curvature, *edge curvature*. Suppose $[v_i, v_j, v_k, v_l]$ is a tetrahedron, the dihedral angle on edge e_{ij} is denoted as β_{ij}^{kl}. If edge e_{ij} is an interior edge (i.e. not on the boundary surface), its edge curvature is defined as

$$K(e_{ij}) = 2\pi - \sum_{kl} \beta_{ij}^{kl}.$$

If e_{ij} is on the boundary surface, its curvature is defined as

$$K(e_{ij}) = \pi - \sum_{kl} \beta_{ij}^{kl}.$$

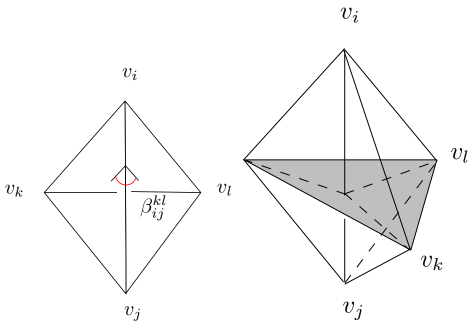

Fig. 16. Discrete edge curvature for a 3-manifold.

It turns out that edge curvature is more essential for 3-manifolds than vertex curvature. The later is determined by the former.

Theorem Suppose M is a tetrahedron mesh, v_i is an interior vertex of M. Then

$$\sum_j K(e_{ij}) = K(v_i).$$

Discrete Curvature Flow Given a hyperbolic tetrahedron in $\mathbb{H}^3$ with edge lengths x_{ij} and dihedral angles θ_{ij}, the *volume* of the tetrahedron V is a function of the dihedral angles $V = V(\theta_{12}, \theta_{13}, \theta_{14}, \theta_{23}, \theta_{24}, \theta_{34})$, and the Schlaefli formula can be expressed as

$$\frac{\partial V}{\partial \theta_{ij}} = \frac{-x_{ij}}{2}. \tag{31}$$

Namely, the differential 1-form dV is $\frac{-1}{2}\sum_{ij} x_{ij} d\theta_{ij}$. It can be further proved that the volume of a hyperbolic truncated tetrahedron is a strictly concave function of the dihedral angles.

If a 3-manifold is approximated by a set of truncated tetrahedra, we say that it is *ideally triangulated*. Given an ideally triangulated 3-manifold (M, T), let E be the set of edges in the triangulation. An assignment $x : E \to \mathbb{R}^+$ is called a *hyperbolic cone metric associated with the triangulation* T if for each tetrahedron t in T with edges $e_1, e_2, \cdots, e_6$, the $x(e_i)$ are the edge lengths of a hyperbolic truncated tetrahedron in $\mathbb{H}^3$. The set of all hyperbolic cone metrics associated with T is denoted as $L(M, T)$, which is an open set. The discrete curvature of a cone metric is a map $K(x) : L \to R$, mapping each edge e to its discrete curvature. The discrete curvature flow is then defined by

$$\frac{dx_{ij}}{dt} = K_{ij}, \tag{32}$$

where x_{ij} is the edge length of e_{ij}, K_{ij} is the edge curvature of e_{ij}. The curvature flow is the gradient flow of the function V over M,

$$V(\mathbf{x}) = \int_{\mathbf{x}_0}^{\mathbf{x}} \sum_{e_{ij}} K_{ij} dx_{ij}, \tag{33}$$

where $\mathbf{x}_0$ is the initial metric, which can be set to $(1, 1, \cdots, 1)$.

Theorem 7. *The equilibrium points of the discrete curvature flow Eqn.32 are the complete hyperbolic metric with totally geodesic boundary. Each equilibrium is a local attractor of the flow.*

Furthermore, a hyperbolic cone metric associated with an ideal triangulation is locally determined by its cone angles. For any ideal triangulated 3-manifold, under the discrete curvature flow, the discrete curvature $K_{ij}(t)$ evolves based on the discrete heat equation. Furthermore, the total curvature $\sum_{ij} K_{ij}^2$ is strictly decreasing until all edge curvatures (and hence all the vertex curvatures) are zeros. The theoretic proofs can be found in [Luo05].

7 Algorithm of Discrete Curvature Flow for Hyperbolic 3-Manifolds

The input to the algorithm is the boundary surface of a 3-manifold, represented as a triangular mesh. The output is a realization (i.e. fundamental domain) of the 3-manifold in the hyperbolic space $\mathbb{H}^3$. The algorithm pipeline is as the following; more details can be found in [YJLG08].
1. Compute a triangulation of the 3-manifold as a tetrahedral mesh. Simplify the triangulation such that the number of the tetrahedra is minimal.
2. Run discrete curvature flow on the tetrahedral mesh to obtain the hyperbolic metric.
3. Realize the mesh in the hyperbolic space $\mathbb{H}^3$ using the computed hyperbolic metric .

7.1 Triangulation and Simplification

Given the boundary surface of a 3-manifold, there are existing methods to tessellate the interior and construct the tetrahedral mesh. In this work, we use tetrahedral tessellation based on volumetric Delaunay triangulation.

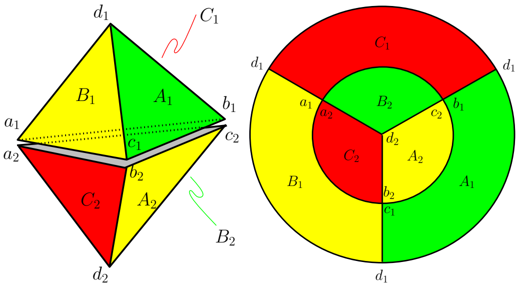

Fig. 17. Simplified triangulation and gluing pattern of Thurston's knotted-Y. The two faces with the same color are glued together.

The following algorithm will simplify the triangulation to a minimum number of truncated tetrahedra.

1. Denote the boundary of a 3-manifold M as $\partial M = \{S_1, S_2, \cdots, S_n\}$. For each boundary surface component S_i, create a cone vertex v_i; for each triangle face $f_j \in S_i$, create a new tetrahedron T_j^i whose vertex set consists of v_i and the vertices of f_j. In this way, M is augmented with a set of cone vertices and a set of new tetrahedra.
2. Use *edge collapse* as shown in Fig.18 to simplify the triangulation, such that all vertices are removed except for those cone vertices $\{v_1, v_2, \cdots, v_n\}$ inserted in the previous step. Denote the simplified tetrahedral mesh as $\tilde{M}$.

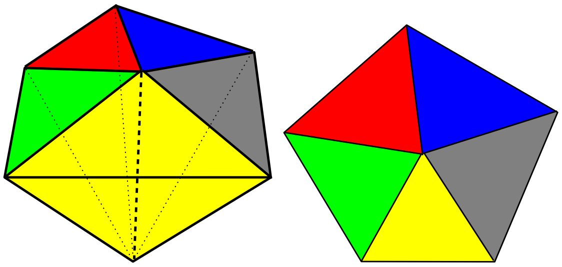

Fig. 18. Edge collapse in tetrahedron mesh.

3. For each tetrahedron $\tilde{T}_i \in \tilde{M}$, cut it with the original boundary surface, remove the parts containing cone vertices, and thus make it a truncated tetrahedron (hyper ideal tetrahedron), denoted as T_i.

The simplified triangulation is represented as a collection of truncated tetrahedra and their gluing pattern. For the example in Fig.17, the simplified tetrahedral mesh consists of only two truncated tetrahedra T_1, T_2. Let A_i, B_i, C_i, D_i represent the four faces of the tetrahedron T_i; a_i, b_i, c_i, d_i represent the truncated vertices of T_i. The gluing pattern is given as follows:

$$\begin{array}{l} A_1 \rightarrow B_2 \ \{b_1 \rightarrow c_2, d_1 \rightarrow a_2, c_1 \rightarrow d_2\} \\ B_1 \rightarrow A_2 \ \{c_1 \rightarrow b_2, d_1 \rightarrow c_2, a_1 \rightarrow d_2\} \\ C_1 \rightarrow C_2 \ \{a_1 \rightarrow a_2, d_1 \rightarrow b_2, b_1 \rightarrow d_2\} \\ D_1 \rightarrow D_2 \ \{a_1 \rightarrow a_2, b_1 \rightarrow c_2, c_1 \rightarrow b_2\} \end{array}$$

The first row means that face $A_1 \in T_1$ is glued with $B_2 \in T_2$ by identifying b_1 with c_2, d_1 with a_2 and c_1 with d_2. Other rows can be interpreted in the same way.

7.2 Hyperbolic Embedding of 3-Manifolds

Once the edge lengths of the tetrahedral mesh are obtained, we can realize it in the hyperbolic space $\mathbb{H}^3$. First, we introduce how to construct a single truncated tetrahedron; then we explain how to glue multiple truncated tetrahedra by hyperbolic rigid motion.

Construction of a Truncated Hyperbolic Tetrahedron The geometry of a truncated hyperbolic tetrahedron is determined by its dihedral angles. This section explains the algorithm to construct a truncated tetrahedron in the upper half space model of $\mathbb{H}^3$. The algorithm consists of two steps. First, construct a circle packing on the plane; second, compute a CSG (Constructive Solid Geometry) surface. The resulting surface is the boundary of the truncated tetrahedron.

Construct a Circle Packing Suppose the dihedral angles of a truncated tetrahedron are given. The tetrahedron can be realized in $\mathbb{H}^3$ uniquely, up to rigid motion. The tetrahedron is the intersection of half spaces, the boundaries of these half spaces are the hyper planes on faces f_1, f_2, f_3, f_4 and the cutting planes at the vertices v_1, v_2, v_3, v_4. Each plane intersects the infinity plane at a hyperbolic line, which is a Euclidean circle on the xy-plane. By abusing the symbols, we use f_i to represent the intersection circle between the hyperbolic plane through the face f_i and the infinity plane. Similarly, we use v_j to represent the intersection circle between the cutting plane at v_j and the infinity plane. The goal of this step is to find planar circles (or lines) f_i's and v_j's, such that
1. f_i and circle f_j intersect at the given corresponding angle β_{ij}^{kl}.
2. circle v_i is orthogonal to circles f_j, f_k, f_l.

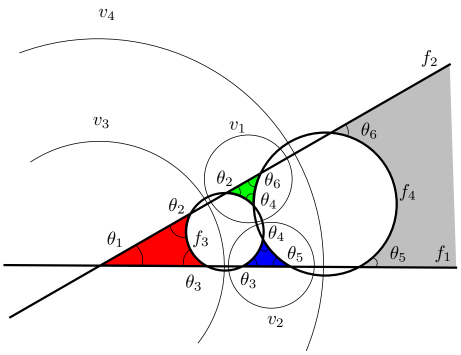

Fig. 19. Circle packing for the truncated tetrahedron.

As shown in Fig.19, all the circles can be computed explicitly with two extra constraints, f_1 and f_2 are lines with two intersection points 0 and ∞, the radius of f_3 equals to one. The dihedral angle on edges $\{e_{34}, e_{14}, e_{24}, e_{12}, e_{23}, e_{13}\}$ are $\{\theta_1, \theta_2, \theta_3, \theta_4, \theta_5, \theta_6\}$ as shown in Fig.14.

After finding v_1, v_2, v_3, v_4, we transform them back using ϕ. Let w_1, w_2, w_3 be points on the circle v_1, the $\phi(w_1), \phi(w_2), \phi(w_3)$ are the points on the circle $\phi(v_1)$.

CSG Modeling After we obtain the circle packing, we can construct hemispheres whose equators are those circles. If the circle is a line, then we construct a half plane orthogonal to the xy-plane through the line. Computing CSG among these hemispheres and half-planes, we can get the truncated tetrahedron as shown in Fig.20.

Each hemisphere is a hyperbolic plane, and separates $\mathbb{H}^3$ to two half-spaces. For each hyperbolic plane, we select one half-space; the intersection of all such half-spaces is the desired truncated tetrahedron embedded in $\mathbb{H}^3$. We need to determine which half-space of the two is to be used. We use f_i to represent both

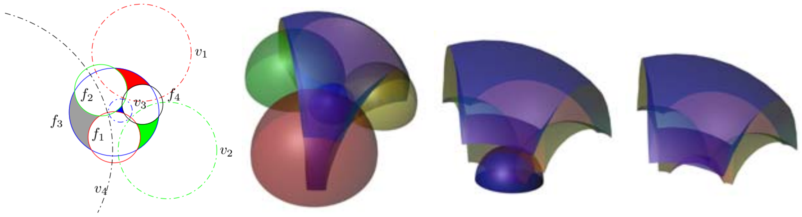

Fig. 20. Constructing an ideal hyperbolic tetrahedron from circle packing using CSG operators.

the face circle and the hemisphere whose equator is the face circle f_i. Similarly, we use v_k to represent both the vertex circle and the hemisphere whose equator is the vertex circle. As shown in Fig.19, three face circles f_i, f_j, f_k bound a curved triangle Δ_{ijk}, which is color coded, one of them is infinite. If Δ_{ijk} is inside the circle f_i, then we choose the half space inside the hemisphere f_i; otherwise we choose the half-space outside the hemisphere f_i. Suppose vertex circle v_k is orthogonal to the face circles f_i, f_j, f_k; if Δ_{ijk} is inside the circle v_k, then we choose the half-space inside the hemisphere v_k; otherwise we choose the half-space outside the hemisphere v_k.

Fig.21 demonstrates a realization of a truncated hyperbolic tetrahedron in the upper half space model of $\mathbb{H}^3$, based on the circle packing in Fig.19.

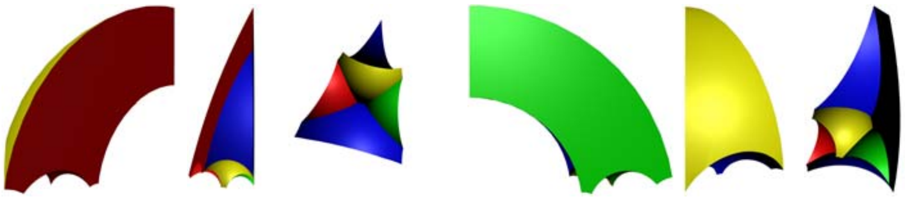

Fig. 21. Realization of a truncated hyperbolic tetrahedron in the upper half space model of $\mathbb{H}^3$, based on the circle packing in figure 19.

Glue two Truncated Hyperbolic Tetrahedra Suppose we want to glue two truncated hyperbolic tetrahedra, T_1 and T_2, along their faces. We need to specify the correspondence between the vertices and faces between T_1 and T_2. As shown in Fig.22, suppose we want to glue $f_4 \in T_1$ to $f_l \in T_2$, such that $\{v_1, v_2, v_3\} \subset T_1$ are attached to $\{v_i, v_j, v_k\} \subset T_2$. Such a gluing pattern can be denoted as a permutation $\{1,2,3,4\} \to \{i,j,k,l\}$. The right-angled hyperbolic hexagon of f_4 is congruent to the hexagon of f_l.

As shown in Fig.23, the gluing can be realized by a rigid motion in $\mathbb{H}^3$, which induces a Möbius transformation on the xy-plane. The Möbius transformation aligns the corresponding circles, $f_3 \to f_4$, $\{v_1, v_2, v_4\} \to \{v_1, v_2, v_3\}$. The Möbius

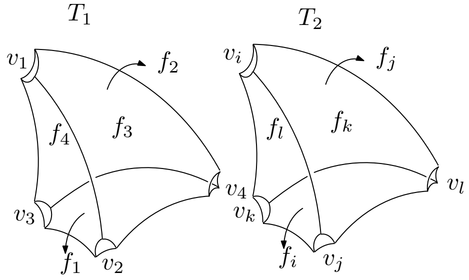

Fig. 22. Glue T_1 and T_2 along $f_4 \in T_1$ and $f_l \in T_2$, such that $\{v_1, v_2, v_3\} \subset T_1$ are attached to $\{v_i, v_j, v_k\} \subset T_2$.

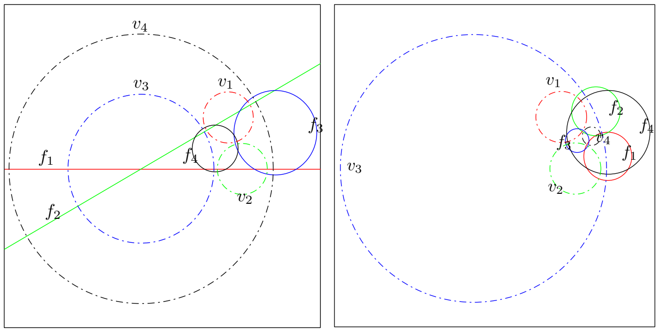

Fig. 23. Glue two tetrahedra by using a Möbius transformation to glue their circle packings, such that $f_3 \to f_4$, $v_1 \to v_1, v_2 \to v_2, v_4 \to v_3$.

transformation can be explicitly computed, and determines the rigid motion in $\mathbb{H}^3$.

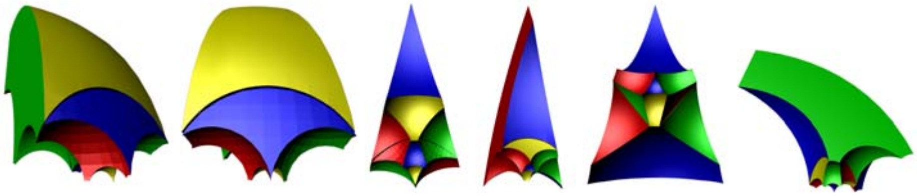

Fig. 24. Glue T_1 and T_2. Frames (a)(b)(c) show different views of the gluing $f_3 \to f_4$, $\{v_1, v_2, v_4\} \to \{v_1, v_2, v_3\}$. Frames (d) (e) (f) show different views of the gluing $f_4 \to f_3$,$\{v_1, v_2, v_3\} \to \{v_2, v_1, v_4\}$.

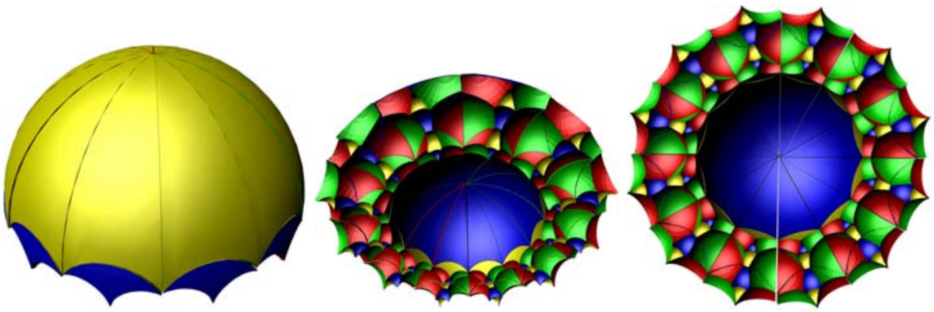

Fig. 25. Embed the 3-manifold periodically in the hyperbolic space $\mathbb{H}^3$.

Fig.24 shows the gluing between two truncated hyperbolic tetrahedra. By repeating the gluing process, we can embed the universal covering space of the hyperbolic 3-manifold in $\mathbb{H}^3$. Fig.25 shows different views of the embedding of the (finite portion) universal covering space of Thurston's knotted Y-Shape in $\mathbb{H}^3$ with the hyperbolic metric.

7.3 Future Work

Designing discrete curvature flow algorithms for general 3-manifolds is a challenging problem. The rigorous algorithms lead to a discrete version of a constructive proof of the Poincaré's conjecture and Thurston's geometrization conjecture. One of the approach is to study the property of the map from the edge length to the edge curvature. If the map is globally invertible, then one can design metrics by curvatures. If the map is locally invertible, then by carefully choosing a special path in the curvature space, one can design metrics by special curvatures.

One of the major difficulties is to verify whether the prescribed curvature is admissible by the mesh. The degenerated tetrahedra will emerge in the process of the curvature flow. The understanding of the formation of the degeneracies will be the key to design the discrete 3-manifold curvature flow.

References

[AMD02] Pierre Alliez, Mark Meyer, and Mathieu Desbrun. Interactive geometry remeshing. *SIGGRAPH 2002*, pages 347–354, 2002.

[Aub76] Thierry Aubin. Équations diffréntielles non linéaires et problème de yamabe concernant la courbure scalaire. *J. Math. Pures Appl.*, 55(3):269–296, 1976.

[BH03] Philip L. Bowers and Monica K. Hurdal. Planar conformal mapping of piecewise flat surfaces. In *Visualization and Mathematics III*, pages 3–34, Berlin, 2003. Springer-Verlag.

[BS04] Alexander I Bobenko and Boris A Springborn. Variational principles for circle patterns and koebe's theorem. *Transactions of the American Mathematical Society*, 356:659–689, 2004.

[CCG] Computational conformal geometry library 1.1. *http://www.cs.sunysb.edu/˜manifold/CCGL1.1/.*

[Cho91] Bennett Chow. The Ricci flow on the 2-sphere. *J. Differential Geom.*, 33(2):325–334, 1991.

[CJGQ05] Christopher Carner, Miao Jin, Xianfeng Gu, and Hong Qin. Topology-driven surface mappings with robust feature alignment. In *IEEE Visualization 2005*, pages 543–550, 2005.

[CL03] Bennett Chow and Feng Luo. Combinatorial Ricci flows on surfaces. *Journal Differential Geometry*, 63(1):97–129, 2003.

[CS03] Chuck Collins and Kenneth Stephenson. A circle packing algorithm. *Computational Geometry: Theory and Applications*, 25:233–256, 2003.

[dVY91] Colin de Verdiere Yves. Un principe variationnel pour les empilements de cercles. *Invent. Math.*, 104(3):655–669, 1991.

[GHQ06] Xianfeng Gu, Ying He, and Hong Qin. Manifold splines. *Graphical Models*, 68(3):237–254, 2006.

[Gug77] Heinrich W. Guggenheimer. *Differential Geometry.* Dover Publications, 1977.

[GY08] Xianfeng David Gu and Shing-Tung Yau. *Computational Conformal Geometry.* Advanced Lectures in Mathematics. High Education Press and International Press, 2008.

[Ham82] Richard S. Hamilton. Three manifolds with positive Ricci curvature. *Journal of Differential Geometry.*, 17:255–306, 1982.

[Ham88] Richard S. Hamilton. The Ricci flow on surfaces. *Mathematics and general relativity (Santa Cruz, CA, 1986), Contemp. Math. Amer.Math.Soc. Providence, RI*, 71, 1988.

[JKLG08] Miao Jin, Junho Kim, Feng Luo, and Xianfeng Gu. Discrete surface ricci flow. *IEEE Transaction on Visualization and Computer Graphics*, 2008.

[JLYG07] Miao Jin, Feng Luo, Shing-Tung Yau, and Xianfeng Gu. Computing geodesic spectra of surfaces. In *Symposium on Solid and Physical Modeling*, pages 387–393, 2007.

[Koe36] Koebe. Kontaktprobleme der Konformen Abbildung. *Ber. Sächs. Akad. Wiss. Leipzig, Math.-Phys. Kl.*, 88:141–164, 1936.

[KSS06] Liliya Kharevych, Boris Springborn, and Peter Schröder. Discrete conformal mappings via circle patterns. *ACM Trans. Graph.*, 25(2):412–438, 2006.

[LGD07] Feng Luo, Xianfeng Gu, and Junfei Dai. *Variational Principles for Discrete Surfaces*. Advanced Lectures in Mathematics. High Education Press and International Press, 2007.

[LP87] John M. Lee and Thomas H. Parker. The yamabe problem. *Bulletin of the American Mathematical Society*, 17(1):37–91, 1987.

[LPRM02] Bruno Lévy, Sylvain Petitjean, Nicolas Ray, and Jérome Maillot. Least squares conformal maps for automatic texture atlas generation. *SIGGRAPH 2002*, pages 362–371, 2002.

[Luo04] Feng Luo. Combinatorial yamabe flow on surfaces. *Commun. Contemp. Math.*, 6(5):765–780, 2004.

[Luo05] Feng Luo. A combinatorial curvature flow for compact 3-manifolds with boundary. *Electron. Res. Announc. Amer. Math. Soc.*, 11:12–20, 2005.

[Mos68] G. D. Mostow. Quasi-conformal mappings in n-space and the rigidity of the hyperbolic space forms. *Publ.Math.IHES*, 34:53–104, 1968.

[Per02] Grisha Perelman. The entropy formula for the Ricci flow and its geometric applications. Technical Report arXiv.org, November 11 2002.

[Per03a] Grisha Perelman. Finite extinction time for the solutions to the Ricci flow on certain three-manifolds. Technical Report arXiv.org, July 17 2003.

[Per03b] Grisha Perelman. Ricci flow with surgery on three-manifolds. Technical Report arXiv.org, March 10 2003.

[RS87] Burt Rodin and Dennis Sullivan. The convergence of circle packings to the riemann mapping. *Journal of Differential Geometry*, 26(2):349–360, 1987.

[Sch84] Richard Schoen. Conformal deformation of a riemannian metric to constant scalar curvature. *J. Differential Geom.*, 20(2):479–495, 1984.

[SSP08] Boris Springborn, Peter Schröoder, and Ulrich Pinkall. Conformal equivalence of triangle meshes. *ACM Transactions on Graphics*, 27(3):1–11, 2008.

[Thu76] William P. Thurston. *Geometry and Topology of Three-Manifolds*. Princeton lecture notes, 1976.

[Thu80] William P. Thurston. *Geometry and Topology of Three-Manifolds*. lecture notes at Princeton university, 1980.

[Thu85] William P. Thurston. The finite riemann mapping theorem. 1985.

[Tru68] Neil S. Trudinger. Remarks concerning the conformal deformation of riemannian structures on compact manifolds. *Ann. Scuola Norm. Sup. Pisa*, 22(2):265–274, 1968.

[Wei07] Steven H. Weitraub. *Differential Forms: A Complement to Vector Calculus*. Academic Press, 2007.

[Yam60] Hidehiko Yamabe. The yamabe problem. *Osaka Math. J.*, 12(1):21–37, 1960.

[YJLG08] Xiaotian Yin, Miao Jin, Feng Luo, and Xianfeng Gu. Computing and visualizing constant-curvature metrics on hyperbolic 3-manifolds with boundaries. In *4th International Symposium on Visual Computing*, 2008.